Magnetic disorder and gap symmetry in the optimally electron-doped Sr(Fe,Co)₂As₂ superconductor

Luminita Harnagea,[1,*] Giri Mani,[1] Rohit Kumar,[1] and Surjeet Singh[1,2,†]

[1]*Department of Physics, Indian Institute of Science Education and Research, Pune, Maharashtra-411008, India*
[2]*Center for Energy Science, Indian Institute of Science Education and Research, Pune, Maharashtra-411008, India*

We study magnetic pair breaking due to Mn impurities in the optimally electron-doped superconductor $Sr(Fe_{0.88}Co_{0.12})_2As_2$. We found that the as-grown $Sr(Fe_{0.88-y}Co_{0.12}Mn_y)_2As_2$ single crystals exhibit a T_c suppression rate of ~30 mK/$\mu\Omega$ cm. This rate is slow but in good agreement with the previous reports on various magnetic/nonmagnetic impurities doped in other structurally analogous iron-based superconductors. The slow T_c suppression rate for magnetic impurities is often cited as an evidence for the nonvalidity of the s_{++}-wave symmetry, which should have suppressed T_c in accordance with the Abrikosov-Gor'kov theory. Here, we show that the crystallographic defects are the main source of pair breaking in the as-grown crystals. Once these defects are *healed* by a low-temperature annealing, the true T_c suppression rate due to Mn impurities is revealed. We thus estimate the actual T_c suppression rate due to Mn alone to be $\geqslant$325 mK/$\mu\Omega$ cm, and that due to the nonmagnetic crystallographic defects to be nearly 35 mK/$\mu\Omega$ cm. These findings can be reconciled with the fully gapped s_{+-}-wave symmetry provided the interband scattering is rather weak. On the other hand, the s_{++}-wave symmetry, which is resilient to the nonmagnetic defects and fragile against the magnetic impurities, can be a possible pairing symmetry in the optimally electron-doped $SrFe_2As_2$. The crucial information that we provide here is that the magnetic pair breaking in these superconductors is not as weak as is generally believed.

I. INTRODUCTION

The iron-based superconductors (FeSCs) have gathered considerable attention because of their high superconducting transition temperature(s) (T_c) and intriguing superconducting properties (see Refs. [1–6]). Since their discovery about a decade back, a considerable progress has been made towards understanding the normal state and superconducting properties of these materials [1,2]. However, the central question concerning the superconducting order-parameter pairing symmetry has remained contentious until now [7–10]. Unlike the copper-based high-T_c SCs (cuprates), where the d-wave symmetry of the order parameter was unequivocally established within few years of their discovery, no such universal pairing symmetry has been assigned to FeSCs. This is partly because of their complex electronic structure consisting, quite generally, of two or more holelike Fermi sheets around the $\Gamma = (0,0)$ point, and two electronlike Fermi sheets around the $M = (\pi,\pi)$ point of the 2-Fe Brillouin zone.

In literature, one finds various competing proposals concerning the pairing symmetry in FeSCs (for a recent review on this, see Ref. [11]). However, a vast majority of these studies favor a fully gapped s-wave state, which can either be the sign-changing s_{+-} state where antiferromagnetic (AFM) spin fluctuations are involved in the Cooper-pair formation [10,12–16] or a non-sign-changing s_{++} state where the orbital fluctuations are important for the pairing mechanism [17,18]. While both these states have the same symmetry, in the

s_{+-} case the superconducting order parameter changes sign between the hole and electron Fermi sheets, in s_{++} model the sign is preserved. The fully gapped s-wave nature of the superconducting state has also been endorsed by several experiments, including penetration depth [19–22], NMR [23], angle-resolved photoemission spectroscopy (ARPES) [24], and μSR [25]. However, these experiments cannot unambiguously establish whether the gap structure is s_{+-} or s_{++}, which has remained a point of constant ongoing debate [7].

The superconducting pair breaking in the presence of impurities can be a useful way to get around this problem. In a single-band s-wave superconductor, for instance, a magnetic impurity suppresses T_c according to the Abrikosov-Gor'kov (AG) law as $\ln(T_c/T_{c0}) = \psi(1/2) - \psi(1/2 + \gamma/2)$, where T_{c0} is the superconducting transition temperature in the pristine sample, ψ is the digamma function, and $\gamma = \Gamma/\pi T_c$ (see Ref. [26]). Here, Γ is the effective magnetic pair-breaking rate which is proportional to the impurity concentration. To account for T_c suppression in FeSCs due to impurities, this formalism has been extended to the isotropic multiband s-wave superconductors [27]. However, the experimentally observed T_c suppression rates have been found to be almost an order of magnitude slower than what one would expect based on this theory. To resolve this issue, Wang *et al.* (Ref. [28]) argued that a naive comparison of experimentally measured T_c suppression rates with theory in terms of impurity concentration is misleading. They proposed that a more useful way to compare T_c suppression rate is to express it in terms of an increase in the residual resistivity upon doping pointlike scattering centers.

To obtain pointlike scattering centers, recently, Prozorov *et al.* studied electron irradiated superconductor

*luminita@iiserpune.ac.in
†surjeet.singh@iiserpune.ac.in

Ba(Fe$_{1-x}$Ru$_x$)$_2$As$_2$ ($x = 0.24$). They found a T_c suppression rate of about 350 mK/$\mu\Omega$ cm due to the electron irradiated pointlike defects [29], which is almost an order of magnitude larger than previously reported rates with chemically doped impurities. They further showed that the observed T_c suppression rate can be described within the AG framework by considering the interband scattering in the s_{+-}-wave picture. However, in Ba(Fe$_{1-x}$Ru$_x$)$_2$As$_2$, where the substitution of Fe by Ru is an isovalent doping, both types of charge carriers (i.e., electrons and holes) remain equally dominant up to high doping concentrations [30]. Here, we ask what will the pairing be in an optimally electron-doped FeSC whose Fermi surface will have the hole pockets near the center of the Brillouin zone substantially shrunk, and the electron pockets at the zone corners enlarged [31]?

Our investigations are carried on the optimally Co-doped SrFe$_2$As$_2$ single crystals consisting of Mn as the magnetic pair breaker. We show that the T_c suppression rate of approximately 30 mK/$\mu\Omega$ cm in the as-grown single crystals is essentially controlled by the crystallographic defects. While these unintended defects veil the true T_c suppression rate due to Mn impurities, their presence turned out to be of significant importance because of their nonmagnetic and pointlike nature [32], and because of the fact that they can easily be cured by low-temperature annealing. In the annealed crystals, the T_c suppression rate due to Mn impurities is estimated to be $\geqslant 325$ mK/$\mu\Omega$ cm, and that due to the nonmagnetic crystallographic defects to be $\leqslant 35$ mK/$\mu\Omega$ cm. Our experiments, in agreement with previous reports on structurally analogous FeSCs, suggest that the Mn spins are localized, hence the suppression of T_c due to Mn impurities is due to magnetic pair breaking and not due to charge doping. An order of magnitude slower rate of suppression for the nonmagnetic defects than reported by Prozorov *et al.* [29], together with a considerably fast suppression rate due to magnetic impurities, suggest that for the applicability of s_{+-}-wave model the interband to intraband scattering ratio should be significantly smaller. On the other hand, the s_{++}-wave superconductivity which is by nature resilient to nonmagnetic defects and fragile in the presence of magnetic defects is also a possible contender. Thus, one can state that the suppression of T_c is due to magnetic effect rather to the combined effect of charge a spin of the extra electron or hole.

The rest of the paper has been organized as follows. Section II deals with the experimental details, including the single-crystal growth and the annealing treatment. In Sec. III A structural characterizations are presented. Thermopower and magnetization are presented in Sec. III B. Section III C deals with investigation of T_c suppression in the as-grown crystal. The effect of annealing on the T_c suppression is presented under Sec. III D. A discussion of the gap symmetry and pair-breaking mechanism based on results presented in the preceding sections is covered under Sec. IV. This is followed by Sec. V which gives a summary of the important results and conclusions derived from this work.

II. EXPERIMENTAL PROCEDURE

Experiments were carried out on a series of self-flux grown single crystals of compositions Sr(Fe$_{1-x_N-y_N}$Co$_{x_N}$Mn$_{y_N}$)$_2$As$_2$

TABLE I. Chemical formula, nominal (y_N) and the obtained Mn composition using $y = (0.872 \pm 0.013)y_N$. Actual Co concentration (x) in each sample is close to 0.12 (see text for details).

Chemical formula	y_N	y	Short name
SrFe$_2$As$_2$	0	0	Sr122
Sr(Fe$_{0.86}$Co$_{0.14}$)$_2$As$_2$	0	0	Mn0.0
Sr(Fe$_{0.8575}$Co$_{0.14}$Mn$_{0.0025}$)$_2$As$_2$	0.0025	0.002	Mn0.2
Sr(Fe$_{0.855}$Co$_{0.14}$Mn$_{0.005}$)$_2$As$_2$	0.005	0.004	Mn0.4
Sr(Fe$_{0.8525}$Co$_{0.14}$Mn$_{0.0075}$)$_2$As$_2$	0.0075	0.006	Mn0.6
Sr(Fe$_{0.85}$Co$_{0.14}$Mn$_{0.01}$)$_2$As$_2$	0.01	0.009	Mn0.9
Sr(Fe$_{0.845}$Co$_{0.14}$Mn$_{0.015}$)$_2$As$_2$	0.015	0.013	Mn1.3
Sr(Fe$_{0.84}$Co$_{0.14}$Mn$_{0.02}$)$_2$As$_2$	0.02	0.017	Mn1.7
Sr(Fe$_{0.83}$Co$_{0.14}$Mn$_{0.03}$)$_2$As$_2$	0.03	0.026	Mn2.6
Sr(Fe$_{0.81}$Co$_{0.14}$Mn$_{0.05}$)$_2$As$_2$	0.05	0.044	Mn4.4
Sr(Fe$_{0.76}$Co$_{0.14}$Mn$_{0.10}$)$_2$As$_2$	0.10	0.087	Mn8.7
Sr(Fe$_{0.71}$Co$_{0.14}$Mn$_{0.15}$)$_2$As$_2$	0.15	0.131	Mn13

[for $x_N = 0.14$ and $y_N = 0$ to 0.15 (see Table I for values of y_N)]. Here and elsewhere in the paper, the symbols x_N and y_N are used to refer to the nominal Co and Mn compositions, respectively; their corresponding experimental values are denoted as x and y. The weighing, mixing, and grinding of the precursors were carried out in an Ar-filled glove box where the level of moisture and O$_2$ is always maintained below 0.1 ppm. The growth experiments were carried out in two steps. In the first step, precursor materials, namely, FeAs, Co$_2$As, and MnAs were prepared using the method similar to that described in Ref. [33]. Briefly, stoichiometric quantities of high-purity Fe (Alpha Aesar, 99.90%), Co (Alpha Aesar, 99.8%), or Mn (Alpha Aesar, 99.95%) powders were thoroughly ground and mixed with As powder (Alpha Aesar, 99.999%) and filled in alumina crucibles which were loaded in preheated quartz ampules inside the glove box. The ampules were sealed under high vacuum and subsequently heated to a temperature of 700 °C for 10 h before cooling to room temperature. At the end of this reaction, the ampules were transferred inside the glove box where they were cut open to remove the reacted products. These products were regrounded and stored inside the glove box.

In the second step, the metal-arsenic precursors were mixed with Sr metal pieces (Sigma Aldrich, 99.00%). Appropriate quantities of As powder were added to get the desired stoichiometry of Sr: Fe$_{(1-x_N-y_N)}$Co$_{x_N}$Mn$_{y_N}$As$_2 \equiv 1:4$. The excess metal arsenic is used as a self-flux. The growth experiments were carried out in alumina crucibles sealed under vacuum in quartz ampules. The charge was slowly heated to 1100 °C, kept there for 24 h, and thereafter cooled slowly down to 950 °C at a rate of 3.5 °C per hour. After waiting at this temperature for 1 h, the furnace was cooled down to room temperature at a rate of 300 °C per hour. This growth procedure allowed us to obtain solidified cm-size ingots from which single crystals having lateral dimension up to 10 mm and thicknesses up to 0.25 mm were mechanically extracted. Representative images of the grown crystals are shown in the inset of Fig. 1.

The structural phase assessment and lattice parameters of all the as-grown single crystals were obtained using the x-ray powder diffraction technique. For this purpose, fine powders obtained by crushing small single-crystal pieces were
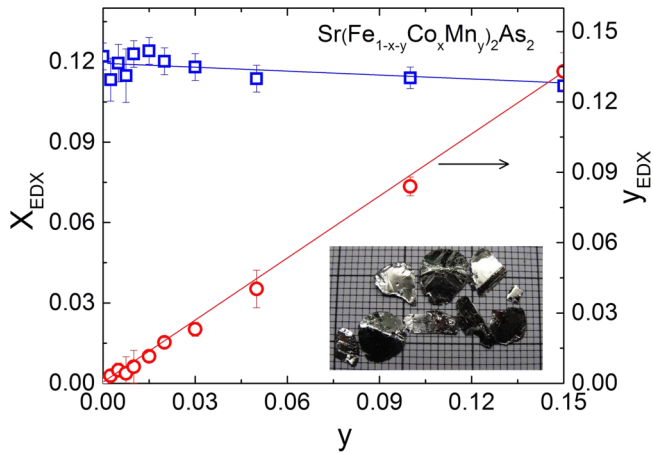
FIG. 1. Co and Mn concentrations determined using the EDX probe, and designated here as x_{EDX} and y_{EDX}, respectively, are plotted against the nominal Mn composition (y). Inset shows a few representative single crystals of SrFe$_2$As$_2$.

used. Measurements were done using a Bruker diffractometer (D8 advanced) equipped with Cu $K\alpha$ radiation. Chemical composition, growth behavior, and morphology of the grown crystals were assessed using a scanning electron microscope (Zeiss Sigma FESEM) equipped with energy dispersive x-ray analysis (EDX) probe. Electrical resistivity was measured from $T = 2$ to 300 K on rectangular plateletlike single crystals, using the standard four-probe technique in a Physical Property Measurement System (PPMS) from Quantum Design. Current (I) and voltage (V) contact were made by gluing gold wires on the sample surface ($\parallel$ ab plane) using a silver epoxy. Magnetization measurements were carried out using a superconducting quantum interference device magnetometer (MPMS XL7) from Quantum Design. Zero-field-cooled (ZFC) and field-cooled (FC) magnetic data were recorded in a temperature range of 2–20 K under an applied magnetic field of 20 Oe. The magnetization data of several samples were also recorded in a temperature interval of 2–300 K under a magnetic field of 10 kOe applied parallel to the crystallographic ab plane. The Seebeck coefficient and Hall measurements were carried out in a PPMS (Quantum Design) using the standard measurement probes.

III. RESULTS

A. Composition and structural analysis of Sr(Fe$_{(1-x_N-y_N)}$Co$_{x_N}$Mn$_{y_N}$)$_2$As$_2$ ($x_N = 0.14, 0 \leqslant y_N \leqslant 0.15$)

The Sr(Fe, Co, Mn)$_2$As$_2$ single crystals exhibit a layered structure with large terraces, nearly micrometer in size, terminating in sharp steps. They tend to cleave easily along the ab plane, and showed tendency towards exfoliation. In order to determine the chemical composition of our single crystals, a few pieces from each growth experiment were analyzed in detail under a SEM. On each specimen, the composition is determined using EDX over 15 to 20 spots. From these data, the average Co and Mn composition is calculated. The statistically averaged composition and standard deviations were used to plot data shown in Fig. 1, where the averaged EDX composition is plotted against the nominal composition. The

standard deviation in each case is found to be less than 0.5%. This value is well within the error bar of the EDX technique and indicates a fairly good homogeneity of Co and Mn distribution within a single crystal, and several single crystals from a given growth experiment. The actual Co composition of our single crystals varied from $x = x_{EDX} \approx 0.11$ to 0.12 (Fig. 1), which is slightly smaller than the nominal value of 0.14. In a previous report on Sr(Fe, Co)$_2$As$_2$ single crystals grown using the self-flux technique, the superconducting dome is reported to extend from $x \approx 0.07$ to 0.17, with a maximum value of T_c around $x \approx 0.117$ (Ref. [34]). Since the variation of T_c near the dome maximum is typically small, a minor variation in the Co concentration for our variously Mn-doped crystals is practically insignificant. The present investigations, therefore, reveal the effect of T_c suppression due to Mn doping in the optimally electron-doped Sr122 superconductor.

As shown in Fig. 1, the Mn concentration obtained using EDX varies linearly as a function of the nominal composition. From a linear fit [solid red line in the Fig. 1 given by $y = y_{EDX} = (0.872 \pm 0.013)y_N$] one can obtain the experimentally determined concentration for any given nominal composition. In the rest of the paper, we will refer to our single crystals by their EDX compositions shown in Table I. The determined chemical formula is Sr(Fe$_{0.88-y}$Co$_{0.12}$Mn$_y$)$_2$As$_2$.

The phase purity of our single crystals and the lattice parameters were determined using x-ray powder diffraction. Several single-crystal pieces from each batch were ground into a fine powder along with silicon, taken as an internal standard; and the diffraction pattern was recorded at room temperature. The samples were found to be single phase and only arbitrarily we observed additional diffraction peaks due to the residual flux, which might have remained on the surface of crystal prior to grinding. The observed powder patterns were indexed based on ThCr$_2$Si$_2$ tetragonal structure, space group $I4/mmm$, No. 139; and the lattice parameters were determined using the UNITCELL refinement software. Additionally, we checked the crystallinity and orientation of the grown crystals by performing x-ray diffraction on cleaved plateletlike crystals in the Bragg-Brentano geometry, which yielded diffraction patterns showing only peaks with Miller indices (0, 0, 2l), indicating that the c axis is perpendicular to the plane of platelets. This was also confirmed using the back-reflection Laue diffraction technique.

The lattice parameters, unit-cell volume, and c/a variation across the Sr(Fe$_{0.88-y}$Co$_{0.12}$Mn$_y$)$_2$As$_2$ series as a function of Mn concentration are shown in Fig. 2. The lattice parameters of SrFe$_2$As$_2$ are found to be $a_0 = 3.928$ Å and $c_0 = 12.354$ Å, in good agreement with previous reports [34,35]. Substitution of Co ($x = 0.12$) for Fe in SrFe$_2$As$_2$ induces a minor increase in the value of a parameter to 3.930 Å, while the c parameter decreases to 12.264 Å. These variations are in agreement with the previous report [34]. Upon substitution of Mn for Fe in Sr(Fe$_{0.88}$Co$_{0.12}$)$_2$As$_2$, the lattice parameters show a gradual increase (Fig. 2). For the crystal with the highest Mn concentration, we found $a/a_0 = 1.002$, $c/c_0 = 1.001$, and $V/V_0 = 1.006$ (where a_0, c_0, V_0 are lattice parameters of SrFe$_2$As$_2$). These trends are in agreement with previous reports on Mn-doped SrFe$_2$As$_2$ and BaFe$_2$As$_2$ series of compounds [36,37], and are also consistent with the differences in the ionic radii, which for the fourfold coordinated Fe^{2+}, Co^{2+}, and
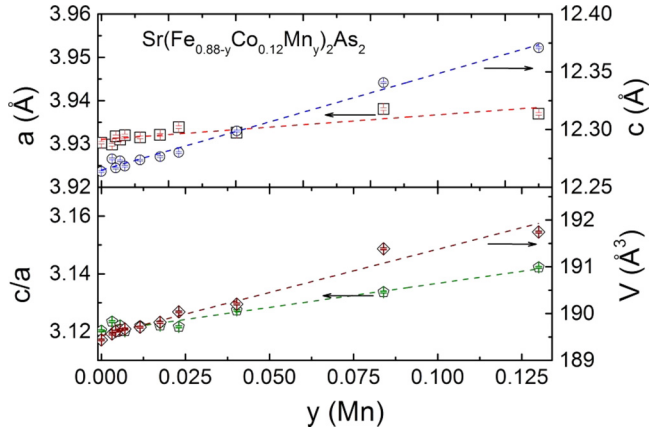
FIG. 2. Lattice parameters a, c, c/a and unit-cell volume V of Sr(Fe$_{0.88-y}$Co$_{0.12}$Mn$_y$)$_2$As$_2$ single crystals plotted as a function of actual Mn concentration (y) (see text for details).

Mn^{2+} is 0.63, 0.58, and 0.66 Å, respectively. Since Mn ion in higher oxidation states has an ionic radius less than 0.58 Å, the observed increase in the unit-cell volume indicates that doped Mn ions are in a +2 oxidation state.

B. Spin and charge state of doped Mn impurities

The temperature (T) dependence of in-plane thermopower (S) of SrFe($_{0.88-y}$Co$_{0.12}$Mn$_y$)$_2$As$_2$ for several representative Mn-doped samples (namely, Mn0.0, Mn2.6, Mn4.4, and Mn13), and for SrFe$_2$As$_2$ (Sr122) is shown in Fig. 3. Thermopower of Sr122 near $T = 300$ K is small and positive ($\sim 3\ \mu$V/K), but it gradually decreases and changes sign when the sample is cooled below $T = 250$ K. Upon further cooling, it changes sign again with a steplike increase to a relatively large and positive value of $12\ \mu$V/K near $T = 190$ K. This temperature coincides with the position of combined structural/magnetic transition previously reported in Sr122 in the resistivity and magnetic susceptibility. The drastic change in S indicates that a significant reconstruction of Fermi surfaces across this transition in agreement with previous Hall and ARPES data [12,38]. Below the transition, thermopower first
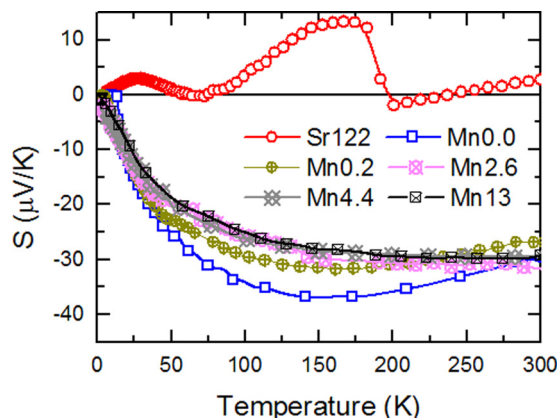

FIG. 3. In-plane Seebeck coefficient (S) of SrFe$_2$As$_2$ and Sr(Fe$_{0.88-y}$Co$_{0.12}$Mn$_y$)$_2$As$_2$ ($y = 0$, 0.002, 0.026, 0.044, 0.13) single crystals plotted as a function of temperature.

decreases to zero (near 60 K) before increasing again resulting in a small hump around 25 K in good agreement with the previous reports [39,40]. Overall, the thermopower behavior of Sr122 is complex, reflecting an interesting interplay of multi-band electronic structure and electron-phonon interactions (phonon drag) in these materials (for a review, see Ref. [41]).

In the optimally Co-doped sample Sr(Fe$_{0.88}$Co$_{0.12}$)$_2$As$_2$ (Mn0.0), the thermopower behavior changes dramatically with respect to the undoped compound (Fig. 3). It now varies smoothly and remains negative over the whole temperature range except in the superconducting state where it becomes zero as expected. The negative sign of thermopower suggests that substituting Co for Fe in SrFe$_2$As$_2$ effectively results in doping electrons in the material, in agreement with the ARPES results [12]. The thermopower attains its maximum negative value of 38 μV/K around $T = 150$ K in good agreement with the optimally Co-doped sample in the Ba(Fe$_{1-x}$Co$_x$)$_2$As$_2$ series [42,43].

With the substitution of Mn, the thermopower remains negative and smoothly varying over the entire temperature range. It decreases slightly with initial Mn doping. This could be due to a possible in-plane anisotropy. What is more interesting here is that the thermopower remains unchanged for samples with different Mn concentrations up to 13% of doping level. This apparent insensitivity of the measured thermopower to increasing Mn-doping level suggests that Mn substitution for Fe does not vary the charge carrier concentration. The temperature variation of Hall coefficient of samples Mn0.0 and Mn2.6, shown in the Supplemental Material, Fig. 1, also supports this conclusion [44].

The localized nature of doped Mn electrons has been also inferred from the magnetization measurements shown in the Supplemental Material (Fig. 3) for samples Sr122, Mn0.0, and Mn13 [44]. A Curie-Weiss analysis of the low temperature χ shows that the doped Mn ions are in a +2 oxidation state with an effective spin $S = \frac{1}{2}$, which corresponds to the low-spin state of Mn in a tetrahedral ligand coordination. This conclusion concerning the spin and charge state of doped Mn ions is consistent with previous angle-resolved photoemission studies (ARPES), nuclear magnetic resonance (NMR), electron spin resonance (ESR), and inelastic neutron scattering studies on Mn-doped BaFe$_2$As$_2$ [45–48].

C. T_c suppression upon Mn doping

The zero-field-cooled (ZFC) and field-cooled (FC) volume susceptibilities (χ_V) of a few representative samples are shown in Fig. 4. Measurements were done under an external magnetic field of 20 ± 5 Oe applied parallel to the ab plane. Transition to a superconducting state upon cooling is evident from the large diamagnetic signals in the ZFC scans shown for samples Mn0.0, M0.4, Mn0.6, and Mn0.9. Sample Mn1.3 shows a superconducting onset near $T = 3$ K but the diamagnetic signal remained very small down to the lowest measurement temperature. No sign of superconductivity is observed in sample Mn1.7 down to $T = 2$ K.

The superconducting transition temperature from χ_V [denoted at $T_c(\chi)$] is obtained as the point of maximum rate change of $\chi(T)$ with respect to temperature below the superconducting onset. Using this criterion, T_c values of 11, 9, 7.5, and 5 K
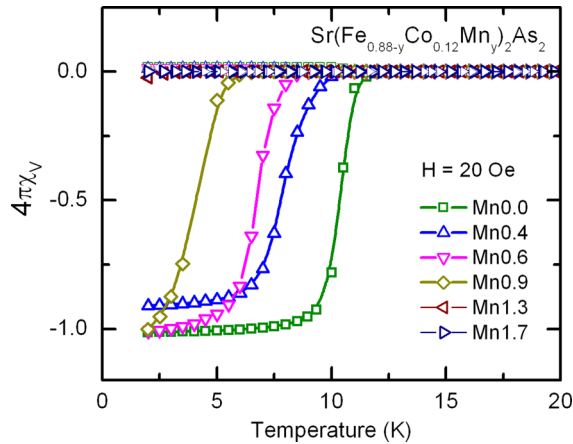
FIG. 4. Temperature dependence of volume susceptibility (χ_V) plotted as $4\pi\chi_V$ for representative Sr(Fe$_{0.88-y}$Co$_{0.12}$Mn$_y$)$_2$As$_2$ ($y = 0$, 0.004, 0.006, 0.009, 0.013, and 0.017) single crystals measured under a field (H) of 20 Oe applied parallel to the surface (*ab* plane) of the platelet-shaped crystals.

FIG. 5. Normalized resistivity $R(T)/R(300$ K$)$ of the as-grown Sr(Fe$_{0.88-y}$Co$_{0.12}$Mn$_y$)$_2$As$_2$ single crystals. Lower panel is an enlarged view of the low-temperature region of (a) showing the superconducting transitions.

are estimated for samples Mn0.0, Mn0.4, Mn0.6, and Mn0.9, respectively. T_c of the sample Mn0.0 is in agreement with previous reports [34]. For all the samples up to 0.9% of Mn doping, the superconducting volume fraction is close to 100% ($4\pi\chi_V \sim -1$). The corrections due to demagnetization factor for plateletlike samples measured here with H ∥ *ab* (Ref. [49]) is estimated to be less than 10%, which ensure bulk superconductivity in samples up to 0.9% of Mn doping. The unsystematic variation in the value of χ_V in the superconducting state is probably due to the residual magnetic field in the magnetometer. For the sample M1.7 the superconducting volume fraction remains marginally small down to 2 K, which indicates that the critical Mn concentration required to quench superconductivity completely in optimally electron-doped Sr122 is close to 1.7 at.%.

We further investigate the T_c suppression using the electrical transport measurements. The temperature variation of normalized in-plane resistivity [$\rho^n(T) = R(T)/R(300K)$], where $R(T)$ is the measured resistance at any temperature T and $R(300$ K$)$ at $T = 300$ K, is shown in Fig. 5. Sample SrFe$_2$As$_2$ exhibits a metallic behavior over the entire temperature range [Fig. 5(a)], with a distinct anomaly near ~192 K (T_o). This anomaly corresponds to the simultaneous structural and magnetic phase transitions from a tetragonal-paramagnetic to an orthorhombic-antiferromagnetic phase upon cooling across T_o (Ref. [35]). The position and steplike appearance of this anomaly is in a good agreement with the previous reports [34,50]. In sample, the optimally Co-doped sample (Mn0.0), the structural/magnetic transition is fully suppressed, which is now replaced by a superconducting transition at low temperatures, as shown in an expanded view in Fig. 5(b). The superconducting transition temperature is determined using the zero-resistance criteria (i.e., the temperature at which the resistance of sample first becomes zero upon cooling). The value of T_c for sample Mn0.0 is found to be 12.5 K, which is in good agreement with the T_c reported by Hu *et al.* [34] for their optimally Co-doped doped Sr122 single crystal grown using the self-flux technique.
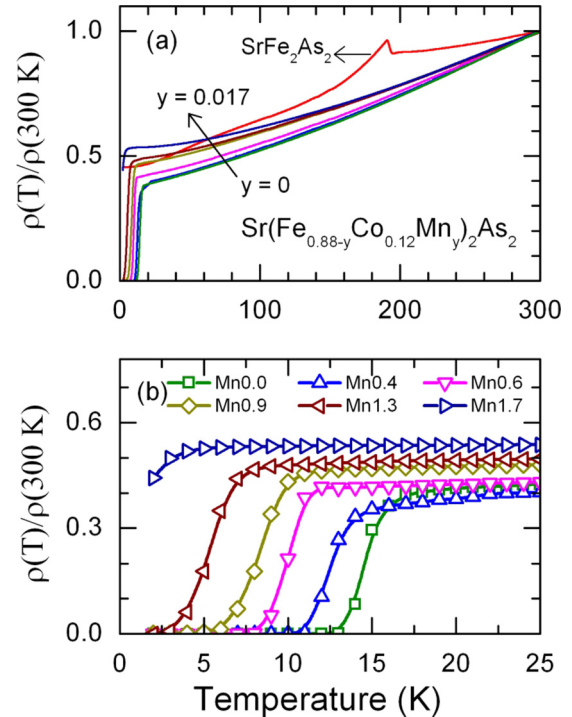
Doping with Mn at the Fe site in Sr(Fe$_{0.88}$Co$_{0.12}$)$_2$As$_2$ results in a gradual suppression of T_c [Fig. 5(b)]. In crystals Mn0.4, Mn0.6, Mn0.9, and Mn1.3, T_c estimated using the zero-resistance criteria has been found to have suppressed to values: 11, 8.5, 5.5, and 2 K, respectively. These values are in close agreement with T_c obtained from the diamagnetic signal in the volume susceptibility. For sample Mn1.7, only a partial drop in resistivity below $T = 3$ K is observed, in agreement with the magnetization data. Superconducting transition width $\triangle T_c$ for these crystals is estimated using $\triangle T_c = T_c^{\text{onset}} - T_c^{\text{zero}}$. Here, T_c^{onset} is the temperature below which the resistivity starts dropping from its normal-state value. The ratio $\triangle T_c/T_c^{\text{mid}}$ where $T_c^{\text{mid}} = (T_c^{\text{onset}} + T_c^{\text{zero}})/2$ for Mn0.0 is about 0.27. This value is comparable to the values previously reported for other FeSCs (see Refs. [34,51] for $\triangle T_c/T_c$ values in Co and Ni-doped Sr122 crystals). This ratio increases with increasing Mn concentration reaching a value of 0.33 for sample Mn0.9. For Mn1.3, this value exceeds 1 due to spurious superconducting onset since χ_V exhibits a SC drop only around 2 K suggesting that $T_c(\chi_V)$ is less than 2 K, as shown in Fig. 4. This broadening of the transition width correlates with the increasing degree of structural disorder associated with random site occupancy of Mn ions replacing the Fe ions in FeAs layers. Additionally, nanoscale inhomogeneities in the Mn concentration across the sample volume cannot be ruled out, which also contributes to the broadening of superconducting transition. We shall return to this point again while discussing the results.

The normalized residual resistivity ratio $\rho_0^n = R(0)/R(300$ K$)$ is obtained by linearly extrapolating the $\rho^n(T)$ curve from the normal region just above T_c to $T = 0$.

TABLE II. Residual resistivity and superconducting transition temperature in the samples $Sr(Fe, Co, Mn)_2As_2$. Residual resistivity ρ_0 ($\mu\Omega$ cm); normalized residual resistivity (ρ_0^n); zero-resistance superconducting onset temperature T_c^{zero} (ρ); superconducting onset temperature (resistivity) $T_c^{onset}(\rho)$; and the superconducting temperature (magnetization) $T_c(\chi)$. In each temperature column the values are in degrees Kelvin. "an" in parentheses indicates annealed crystal.

Name	ρ_0	ρ_0^n	T_c^{zero} (ρ)	$T_c^{onset}(\rho)$	$T_c(\chi)$
Mn0.0	165	0.35	12.5	16.5	11
Mn0.4	170	0.39	11	15	9
Mn0.6	410	0.40	8.5	11.8	7.5
Mn0.9	625	0.45	5.5	10.5	5
Mn1.3	380	0.48	2	7.5	<2
Mn1.7	360	0.53	<2	3	<2
Mn0.0 (an)	35	0.35	17	19.5	16
Mn0.9 (an)	55	0.41	10.5	14.5	10
Mn1.7 (an)	160	0.49	5	11	<2

The value of ρ_0^n is found to increase systematically from 0.35 for Mn0.0 to 0.53 for Mn1.7 sample (see Table II). The variation is depicted graphically in Fig. 6, where % increase in $\rho_0^n [= \triangle \rho_0^n(\%)]$, measured with sample Mn0.0 ($y = 0$) as a reference, is plotted against the Mn concentration [$y(\%)$]. The value of $\rho^n(T)$ for our optimally Co-doped Sr122 crystal is in good agreement with the value of around 0.4 reported by Saha *et al.* for their optimally Ni-doped Sr122 single-crystalline sample [51]. It should be emphasized that had the resistivity curves shifted rigidly up due to Mn impurities, the quantity $\triangle \rho_0^n$ would have been identically zero; its nonzero values therefore signify that the doped Mn impurities cannot be treated as point defects, which is not unexpected but nevertheless worth pointing out.

The absolute value of the residual resistivity (ρ_0) of the superconducting samples is also given in Table II. A residual resistivity value of 165 $\mu\Omega$ cm for sample Mn0.0 compares favorably with a value of around 200 $\mu\Omega$ cm reported previously for an optimally Ni-doped Sr122 (Ref. [51]). With increasing Mn concentration, ρ_0 increases for the superconducting samples. However, for samples Mn1.3 and Mn1.7 it
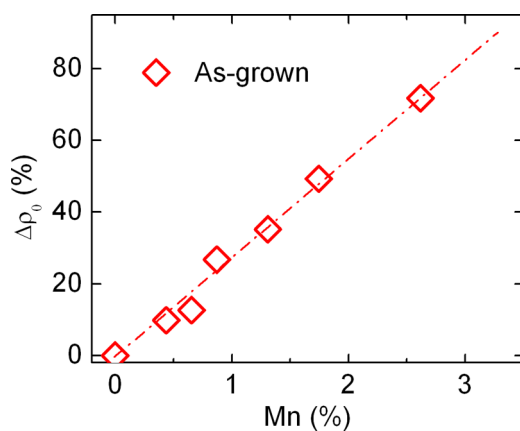

FIG. 6. $\triangle \rho_0(\%)$ plotted as a function of Mn concentration for the superconducting as-grown crystals (see text for details).

decreases. This decrease is probably an experimental artifact since the corresponding ρ_0^n shows only a monotonic increase. A significant error in reducing the measured resistance to resistivity can arise if the width of the individual voltage contacts made using a silver epoxy are larger compared to their separation. The uncertainty in ρ_0 is estimated as the ratio of contact width to the average separation between the contacts. Since shape of the contact is arbitrary, the maximum lateral dimension parallel to sample length is taken as the contact width. Using this method, the estimated error varied from 30% to 50% but the actual errors are expected to be smaller because of the finite conductivity of silver epoxy, and also because of the fact that thickness of the epoxy layer decreases rapidly away from the point where the 25-μm gold wire is actually placed on the sample for making the contact. Both these factors are expected to reduce the effectiveness of voltage probe away from the point where the gold wire is positioned. This will effectively reduce the contact width and increases the separation between contacts, thereby reducing the absolute uncertainty.

To get an estimate of T_c suppression rate in terms of change in the residual resistivity, we considered the variation of ρ_0 from 165 for sample Mn0.0 ($T_c^{zero} = 12.5$ K) to 625 $\mu\Omega$ cm for sample Mn0.9 ($T_c^{zero} \sim 5.5$ K). Using these data we get a T_c suppression rate of nearly 15 mK/$\mu\Omega$ cm which is the same order of magnitude as previously reported for Mn impurities in $Ba_{0.5}K_{0.5}Fe_{2-2x}M_{2x}As_2$ (Ref. [52]). To get an upper bound on the T_c suppression rate, we make an exaggerated estimation of 50% error in the value of ρ_0, which gives a maximum T_c suppression rate of 30 mK/$\mu\Omega$ cm. As pointed out earlier by Prozorov *et al.* (Ref. [29]), this T_c suppression rate is too low to reconcile with the AG theory.

D. Effect of low-temperature annealing on T_c suppression

We now investigate the effect of gently annealing the crystals on T_c suppression rate. Single-crystal specimens of samples Sr122, Mn0.0, Mn0.9, Mn1.7, M4.4, Mn8.7, and Mn13 were annealed at a relatively low temperature of 350 °C for 5 days under vacuum in sealed quartz ampules. As shown in Table II, the residual resistivity values and the superconducting transition temperatures changed significantly upon annealing. We first compare the behavior of sample Sr122 before and after annealing. As shown in Fig. 7(a), the structural/magnetic transition upon annealing increased from 192 to 200 K. The shape of the anomaly associated with this transition also changed, and now matched the peak position and peak shape previously reported for a Sn-flux-grown single crystal [35,36,43]. It is well known that the prolonged annealing at low temperature relieves strain-induced defects. The defect concentration can be particularly high for crystals grown using the self-flux technique due to high processing temperatures involved. Typically, in a growth experiment using the self-flux, the crystal growth ends in the temperature range 900 °C to 950 °C. At this point, the entire charge is cooled to room temperature at a relatively faster rate either by turning off the furnace or by removing the ampule for centrifuging. On the other hand, in a growth experiment involving Sn flux, the low melting point of Sn allows for the crystal growth experiment to proceed down to much lower temperatures (anything between

400 °C to 500 °C), where the crystal is decanted from the flux either by centrifuging or by flipping the ampule containing the charge upside down. Due to the lower processing temperature involved, crystals grown using the Sn flux are expected to have less strain-induced defects than the crystals grown using the self-flux technique, which is probably the reason why a self-flux grown crystal after annealing shows a behavior closer to that of a Sn-grown crystal. EDX analysis of the annealed crystals confirms that no change in the composition takes place due to annealing.

The effect of annealing treatment on the superconducting samples is depicted in Fig. 7(b). The annealing treatment shifts the superconducting transition to higher temperature. For instance, T_c of sample Mn0.0 increases from 12.5 K to almost 17 K after annealing, i.e., an increase of nearly 26%. Simultaneously, the resistivity curve shifts rigidly down due to ρ_0 decreasing from about 165 to 35 $\mu\Omega$ cm. That the resistivity curve is rigidly down-shifted [i.e., through subtraction of a temperature-independent contribution in $\rho(T)$] is apparent from the fact that $\rho^n(T)$ curves for the as-grown and annealed crystals overlap over the whole temperature range as shown in Fig. 7(d). From this observation it can be inferred that the crystallographic defects in the as-grown crystals are pointlike. Strain in FeSCs has been shown to introduce nonmagnetic crystallographic defects analogous to the defects produced by electron irradiation [32]. Even though the concentration of these defects in our as-grown single crystal is not known, an estimation of the T_c suppression due to these defects can be made by considering the change in T_c ($\triangle T_c \approx 4.5$ K) and ρ_0

($\triangle\rho_0 \approx 130$ $\mu\Omega$ cm) solely due to annealing. The quantity $\triangle T_c/\triangle\rho_0$ in this case turns out to be $\sim$35 mK/$\mu\Omega$ cm, which is nearly an order of magnitude smaller than 350 mk/$\mu\Omega$ cm reported by Prozorov *et al.* (Ref. [29]) for their electron irradiated samples consisting of pointlike defects.

We now present the effect of annealing on the T_c of Mn-doped samples. In sample Mn0.9, the value of T_c^{zero} increased by almost 5 K, while the residual resistivity decreased from 625 to roughly 55 $\mu\Omega$ cm. In sample Mn1.7 [Fig. 5(b)], which exhibits a superconducting onset near $T = 3$ K but no zero-resistance state down to 2 K in the as-grown form, now showed a superconducting onset near $T = 11$ K and a transition to the zero-resistance state near $T = 5$ K. The magnetic susceptibility of annealed Mn1.7 also shows onset of superconductivity near $T = 6$ K, but the superconducting volume fraction remains marginal ($\sim$4%) down to $T = 2$ K, and the superconducting transition completely disappeared when measured under a high field of 10 kOe, indicating filamentary superconductivity due to inhomogeneous Mn distribution (see Supplemental Material, Fig. 2) [44]. Similar effect of annealing is manifested by sample M4.4. In its as-grown state, no signs of superconductivity were found down to $T = 2$ K; however, after annealing a superconducting onset was revealed near $T = 10$ K but the zero-resistance state remained out of sight down to 2 K. To check if the high onset temperature is spurious or not, we measured the low-field (20 Oe), in-plane susceptibility which showed no signs of diamagnetic signal down to $T = 2$ K, indicating that the resistive drop is indeed spurious arising from tiny, disconnected puddles of smaller Mn concentration.
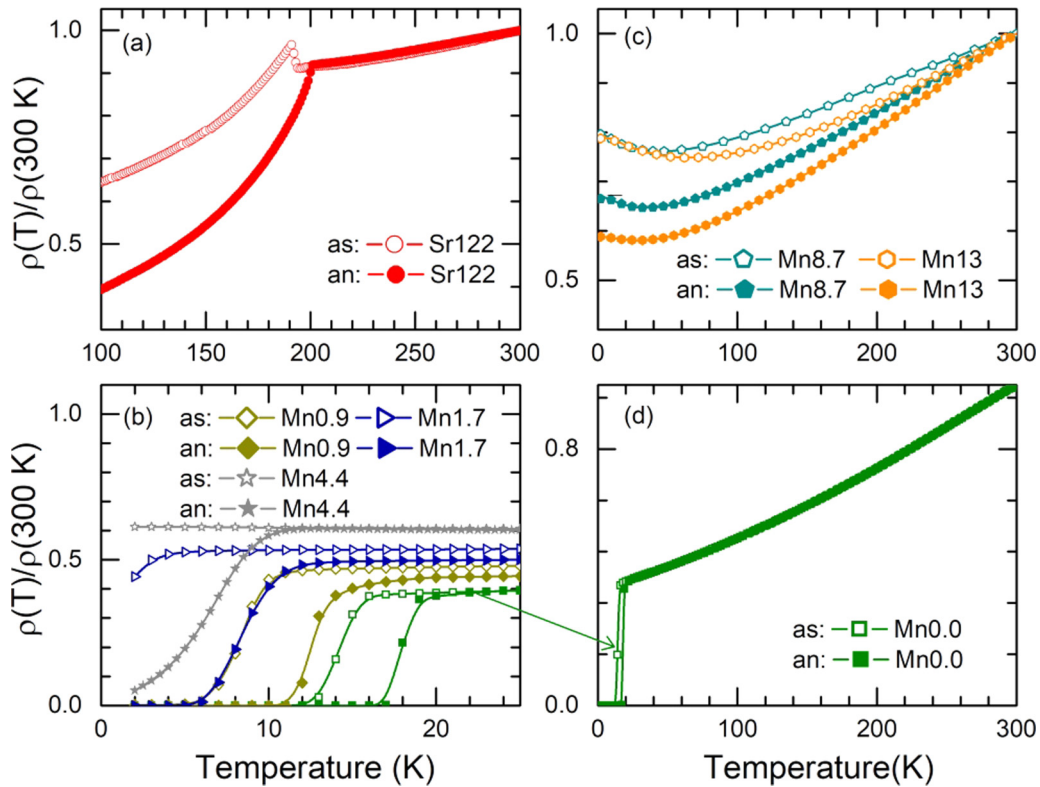

FIG. 7. Normalized resistivity of as-grown (as), annealed (an) single crystals plotted as a function of temperature for SrFe$_2$As$_2$ (a), and Sr(Fe$_{0.88-y}$Co$_{0.12}$Mn$_y$)$_2$As$_2$ (b) and (c). (d) Shows the normalized resistivity of the as-grown and annealed Mn0.0 samples over the whole temperature range.
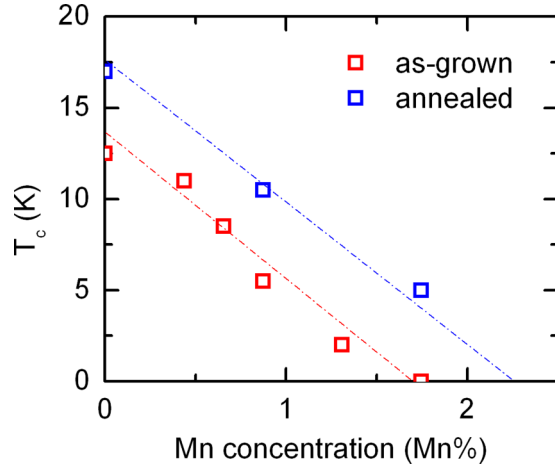
FIG. 8. Plot of T_c as a function of Mn-doping concentration (Mn%) with respect to Fe for the as-grown and annealed crystals.

FIG. 9. T_c suppression rate plotted as a function of Mn concentration expressed as % per Fe. La1111 (Ref. [56]), Ba122-Co $\equiv$ Ba(Fe$_{0.935}$Co$_{0.065}$)$_2$As$_2$ (Ref. [53]), Nd1111(Ref. [57]), Ba122-K (up traingle) $\equiv$ Ba$_{0.5}$K$_{0.5}$Fe$_2$As$_2$ (Ref. [59]), Ba122-K (down triangle) $\equiv$ Ba$_{0.5}$K$_{0.5}$Fe$_2$As$_2$ (Ref. [52]).

These puddles undergo superconducting transition at relatively higher temperatures upon cooling which results in lowering of the resistivity; but since these are disconnected regions, the nonsuperconducting background of the sample does not allow the zero-resistance state to reach.

The occurrence of filamentary or spurious superconducting signal in the annealed samples (Mn1.7 and Mn4.4) may at first sight appear puzzling because the conventional wisdom suggests that annealing homogenizes a sample but here it appears as though annealing has a reverse effect. However, the annealing temperature in our experiments is too low to facilitate any kind of atomic diffusion, therefore, the spatial distribution of Mn should not change due to low-temperature annealing. What low-temperature annealing in effect does is, it relieves the strain-induced crystallographic defects, which lowers the residual resistivity considerably making the spurious superconducting drop perceptible. Interestingly, what this also suggests is that the low-temperature annealing employed here should not have any bearing on the T_c suppression effect due to the magnetic scattering. This is in fact the case as is evident from the plot of T_c versus Mn concentration for the as-grown and annealed crystals shown in Fig. 8. For both sets of samples, the T_c suppression rate is almost equal, but the two T_c versus Mn-concentration lines are shifted by a constant amount which quantifies the effect of pointlike, nonmagnetic crystallographic defects in the as-grown specimens.

The width of superconducting transitions also decreases as a consequence of annealing the samples. For example, in sample Mn0.0, the ratio $\triangle T_c/T_c^{\mathrm{mid}}$ decreases from 0.27 to 0.14 after annealing. In sample Mn0.9, by way of comparison, this ratio decreases from 0.33 to 0.27. The higher value of $\triangle T_c/T_c^{\mathrm{mid}}$ for the Mn-doped crystal even after annealing treatment is due to inhomogeneous Mn distribution, which remains unaffected by the low-temperature annealing.

Finally, we come to the effect of annealing on the non-superconducting samples doped with higher concentrations of Mn. The normalized resistivity of samples Mn8.7 and Mn13 is shown in Fig. 7(c). For these samples the superconductivity is completely suppressed and their resistivity behavior is now characterized by the presence of a shallow low-temperature
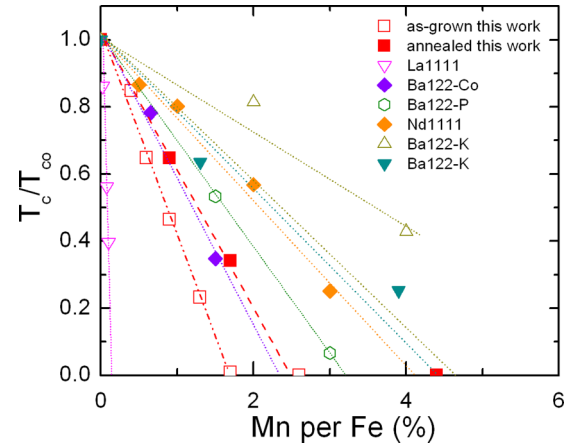
minimum reminiscent of the Kondo effect in the diluted magnetic alloys. At higher Mn concentration, the Mn-Mn interaction mediated via the conduction electrons will also come into play. This new energy scale effectively reorganizes the ground state, expelling superconductivity completely. Interestingly, for the nonsuperconducting samples, the normalized resistivity (ρ^n) after annealing differed considerably from the values in as-grown state, which is different from the superconducting samples where the difference between as-grown and annealed $\rho(T)$ is nearly nonexistent. In future, Raman and infrared studies would be useful to probe changes in the vibrational spectrum of the impurity in annealed samples, which may render useful information concerning the scattering rate.

IV. DISCUSSION

We will now put together the results from the preceding sections to discuss the central question of pairing symmetry in the optimally Co-doped Sr122 superconductor. Our thermopower and Hall data, in line with previous works on Mn substituted FeSCs (see, for example, Refs. [45–47,53,54]), suggest that the d electrons of Mn are localized; and that the charge carrier doping due to Mn substituting Fe in the structure is marginal. Further evidence of the localized nature of Mn d electrons is gathered from the low-temperature magnetization data, which show that the doped Mn ions are in their low-spin state ($S = \frac{1}{2}$), which agrees with the previously inferred spin state using the NMR technique [53]. These results are also in agreement with the spin and charge states of Mn impurities in the superconductor MgB$_2$ [55].

We shall first discuss whether Mn doping in the present investigation has the same quantitative effect on superconducting T_c suppression as reported previously for other FeSCs or not. For this purpose, we plot T_c/T_{c0} as a function of Mn concentration (Mn%) from this study along with data collected from literature for several other FeSCs. The results are shown in Fig. 9. Here, T_{c0} is the superconducting

critical temperature in the absence of Mn impurities. The T_c suppression rates for the various systems shown in Fig. 9 are as follows: $Ba(Fe_{1-x-y}Mn_x)_2(As_{1-y}P_y)_2 = -10$ K/Mn% (Ref. [53]), $Ba(Fe_{1-x-y}Co_xMn_y)_2As_2 = -12$ K/Mn% (Ref. [53]), $Ba_{0.5}K_{0.5}(Fe_{1-x}Mn_x)_2As_2 = -7$ K/Mn% (Ref. [52]), $LaFe_{1-x}Mn_xAs(O, F) = -150$ K/Mn% (Ref. [56]), etc. Leaving aside $LaFe_{1-x}Mn_xAs(O, F)$, in all remaining systems the T_c suppression rates are approximately -7 K/Mn%. The case of $LaFe_{1-x}Mn_xAs(O, F)$ is exceptional where a very steep, almost an order of magnitude faster, T_c suppression rate was reported [56,57]. This behavior, which has been dubbed as the "poisoning effect," is believed to arise as a consequence of strong electronic correlations unique to this system among the FeSC families [58].

The T_c suppression rate of our as-grown and annealed crystals when plotted as function of Mn concentration shows a good overall agreement with the data taken from available literature. This gives an impression that all the FeSCs should have the same gap symmetry, which is now generally believed to s_{+-}. However, as pointed out by Wang *et al.*, in the multiband superconductors a more appropriate way of appraising the pair-breaking effect of a certain impurity is by plotting the T_c suppression rate in terms of increase in the residual resistivity, i.e., by how much will the T_c decreases if residual resistivity increases by 1 $\mu\Omega$ cm upon incorporation of a certain impurity. This can be understood based on the Abrikosov-Gor'kov formalism, where the superconducting transition temperature in the presence of impurities is governed by the impurity scattering rate [26]. Since the scattering rate itself cannot be directly measured in the experiments, residual resistivity increase ($\Delta\rho_0$) in the presence of impurity doping can be used to assess the pair-breaking rate due to a certain impurity. However, these criteria can be compared on a quantitative basis provided the impurities are pointlike; i.e., the $\rho(T)$ curve shifts rigidly upon impurity doping. We show that the normalized resistivity $[R(T)/R(300\,\text{K})]$ of the as-grown and annealed Mn0.0 crystal overlaps completely in the normal state above the superconducting transition, which suggests that the resistivity curve upon annealing exhibits a rigid down-shift as expected for the pointlike defects. We can, therefore, conclude that the as-grown crystal contains pointlike crystallographic defects and that these defects can be effectively healed by a low-temperature annealing procedure. This conclusion is in line with the conclusion reached by Kim *et al.* (Ref. [32]) that the strain-induced crystallographic defects in an optimally Co-doped Sr122 are analogous to the nonmagnetic, point defects created due to electron irradiation. We next discuss how this information can be exploited for extracting the gap structure.

In our optimally Co-doped Sr122 crystal, the T_c suppression due to crystallographic defects was quantified as 35 mK/$\mu\Omega$ cm (see Sec. III D). Intriguingly, this value is nearly an order of magnitude slower than for the electron irradiated $Ba(Fe_{1-x}Ru_x)_2As_2$ where a T_c suppression rate of ≈ 350 mK/$\mu\Omega$ cm was obtained. This was shown to be consistent with the s_{+-}-wave pairing symmetry. Can the observed slow T_c suppression rate due to nonmagnetic defects found here be reconciled with the s_{+-}-wave model is a question which can be answered by investigating the pair-breaking rate due to the Mn impurities.

The actual suppression rate due to Mn is not directly accessible because of unknown amount of residual crystallographic disorder present in the annealed samples; nevertheless, one can try to find a lower bound on it by assuming that in the annealed crystals the only source of pair breaking is Mn impurities (i.e., the crystallographic defects are completely healed). The absolute value of ρ_0 for samples Mn0.0 and Mn0.9 is 35 and 55 $\mu\Omega$ cm, respectively. Their corresponding T_c^0's are 17 and 10.5 K, which yields an approximate value of 325 mK/$\mu\Omega$ cm as the T_c suppression rate in the annealed crystals. That is, in our as-grown crystals, the T_c suppression rate is around 30 mK/$\mu\Omega$ cm, which increases to 325 mK/$\mu\Omega$ cm in the annealed crystals. On the other hand, the T_c suppression rate due to crystallographic defects is estimated to about 35 mK/$\mu\Omega$ cm. From these observations it is obvious that the T_c suppression in the as-grown crystals is controlled by the crystallographic defects. It is only after these defects have been healed that the *true* T_c suppression rate due to magnetic impurities can be assessed.

What can we infer from this analysis? Given a very slow pair-breaking rate due to crystallographic defects, together with our finding that the actual T_c suppression rate due to magnetic impurities is almost an order of magnitude faster, suggest that for the s_{+-}-wave pairing symmetry to prevail the interband scattering should be very weak. The s_{++} state, on the other hand, suits the present situation better since it is fragile against the magnetic impurities and robust against the nonmagnetic impurities. This fragility of s_{++} against magnetic scattering is due to the fact that scattering between the bands with the same sign of the order parameter is equivalent to the magnetic scattering in the conventional s-type BCS superconductors, which follows the Abrikoso-Gor'kov rate [26]. On may argue that in the s_{++}-wave model, due to the crystallographic defects, T_c should not have suppressed at all as opposed to the slow suppression observed here. However, in the s_{++} scenario, a slow T_c suppression may occur if either the gaps are of unequal size and/or the gap structure is slightly anisotropic, none of these possibilities can be completely ruled out here.

V. SUMMARY AND CONCLUSIONS

The main focus of this paper is to investigate the pair breaking due to magnetic impurities to deduce the gap symmetry. In previous works, T_c suppression rates for various transition-metal impurities were found to be slow and essentially independent of the magnetic state of the impurity. This result is often cited in the literature as an evidence for the s_{+-}-wave state. We investigated magnetic pair breaking in optimally electron-doped $SrFe_2As_2$ in the presence of various concentrations of Mn impurities. We show that the pair-breaking rate measured in mK/$\mu\Omega$ cm agrees fairly well with previous reports on Mn doping in analogous superconductors. However, annealing the crystals carefully at low temperature for several days revealed information crucial to the determination of pairing symmetry. We show that the strain-induced crystallographic defects are a major cause of pair breaking in the as-grown crystals. We first established that these defects are pointlike by showing that their effect is to add a temperature-independent scattering term that shifts the entire resistivity curve rigidly. We then estimate

the T_c suppression rate due to these defects and found it to be roughly $\sim$35 mK/$\mu\Omega$ cm. However, in the annealed crystals, where the crystallographic defects are healed to a large extent, T_c suppression rate is found to increase by a factor of 9 or so, which gives a lower bound on the magnetic pair-breaking rate due to Mn impurities. Interestingly, in both sets of crystals (i.e., as-grown and annealed), the T_c suppression rate measured in terms of doping concentration (%Mn) remained unchanged, only the lines in the T_c versus %Mn plot shifted by a constant value due to the pointlike crystallographic defects.

In summary, we provide evidence that the s_{++} symmetry cannot be ruled out in the present case, which suggests that the gap symmetry may indeed vary within the FeSCs families depending on the details of the band structure. We show that a simple heat treatment procedure can provide useful information concerning the gap symmetry by healing the crystallographic defects that should be taken in account while quantifying the relation between T_c suppression rate and the doping level. Our finding that the magnetic pair breaking in FeSCs is much stronger than was previously thought is crucial information for the future theoretical work. In future, similar annealing experiments with other magnetic/nonmagnetic impurities will be quite useful.

[1] H. Hosono and K. Kuroki, Phys. C (Amsterdam) **514**, 399 (2015).

[2] A. V. Chubukov and P. J. Hirschfeld, Phys. Today **68** (6), 46 (2015).

[3] G. R. Stewart, Rev. Mod. Phys. **83**, 1589 (2011).

[4] D. C. Johnston, Adv. Phys. **59**, 803 (2010).

[5] J. Paglione and R. L. Greene, Nat. Phys. **6**, 645 (2010).

[6] K. Ishida, Y. Nakai, and H. Hosono, J. Phys. Soc. Jpn. **78**, 062001 (2009).

[7] Y. Bang and G. R. Stewart, J. Phys.: Condens. Matter **29**, 123003 (2017).

[8] M. M. Korshunov, Y. N. Togushova, and O. V. Dolgov, Phys. Usp. **59**, 1211 (2017).

[9] J. Li, Y.-F. Guo, Z.-R. Yang, K. Yamaura, E. Takayama-Muromachi, H.-B. Wang, and P.-H. Wu, Supercond. Sci. Technol. **29**, 053001 (2016).

[10] P. J. Hirschfeld, M. M. Korshunov, and I. I. Mazin, Rep. Prog. Phys. **74**, 124508 (2011).

[11] P. J. Hirschfeld, C. R. Phys. **17**, 197 (2016).

[12] J. Zhang, R. Sknepnek, R. M. Fernandes, and J. Schmalian, Phys. Rev. B **79**, 220502 (2009).

[13] I. I. Mazin, D. J. Singh, M. D. Johannes, and M. H. Du, Phys. Rev. Lett. **101**, 057003 (2008).

[14] A. V. Chubukov, D. V. Efremov, and I. Eremin, Phys. Rev. B **78**, 134512 (2008).

[15] V. Cvetkovic and Z. Tesanovic, Phys. Rev. B **80**, 024512 (2009).

[16] A. F. Kemper, T. A. Maier, S. Graser, H.-P. Cheng, P. J. Hirschfeld, and D. J. Scalapino, New J. Phys. **12**, 073030 (2010).

[17] H. Kontani and S. Onari, Phys. Rev. Lett. **104**, 157001 (2010).

[18] S. Onari and H. Kontani, Phys. Rev. Lett. **109**, 137001 (2012).

[19] K. Hashimoto, T. Shibauchi, T. Kato, K. Ikada, R. Okazaki, H. Shishido, M. Ishikado, H. Kito, A. Iyo, H. Eisaki *et al.*, Phys. Rev. Lett. **102**, 017002 (2009).

[20] R. T. Gordon, N. Ni, C. Martin, M. A. Tanatar, M. D. Vannette, H. Kim, G. D. Samolyuk, J. Schmalian, S. Nandi, A. Kreyssig, A. I. Goldman *et al.*, Phys. Rev. Lett. **102**, 127004 (2009).

[21] R. T. Gordon, H. Kim, N. Salovich, R. W. Giannetta, R. M. Fernandes, V. G. Kogan, T. Prozorov, S. L. Bud'ko, P. C.

Canfield, M. A. Tanatar, and R. Prozorov, Phys. Rev. B **82**, 054507 (2010).

[22] H. Kim, R. T. Gordon, M. A. Tanatar, J. Hua, U. Welp, W. K. Kwok, N. Ni, S. L. Bud'ko, P. C. Canfield, A. B. Vorontsov, and R. Prozorov, Phys. Rev. B **82**, 060518 (2010).

[23] A. Kawabata, S. C. Lee, T. Moyoshi, Y. Kobayashi, and M. Sato, J. Phys. Soc. Jpn. **77**, 103704 (2008).

[24] H. Ding, P. Richard, K. Nakayama, K. Sugawara, T. Arakane, Y. Sekiba, A. Takayama, S. Souma, T. Sato, T. Takahashi *et al.*, Europhys. Lett. **83**, 47001 (2008).

[25] H. Luetkens, H.-H. Klauss, R. Khasanov, A. Amato, R. Klingeler, I. Hellmann, N. Leps, A. Kondrat, C. Hess, A. Köhler *et al.*, Phys. Rev. Lett. **101**, 097009 (2008).

[26] A. V. Balatsky, I. Vekhter, and J.-X. Zhu, Rev. Mod. Phys. **78**, 373 (2006).

[27] D. V. Efremov, M. M. Korshunov, O. V. Dolgov, A. A. Golubov, and P. J. Hirschfeld, Phys. Rev. B **84**, 180512 (2011).

[28] Y. Wang, A. Kreisel, P. J. Hirschfeld, and V. Mishra, Phys. Rev. B **87**, 094504 (2013).

[29] R. Prozorov, M. Kończykowski, M. A. Tanatar, A. Thaler, S. L. Bud'ko, P. C. Canfield, V. Mishra, and P. J. Hirschfeld, Phys. Rev. X **4**, 041032 (2014).

[30] F. Rullier-Albenque, D. Colson, A. Forget, P. Thuéry, and S. Poissonnet, Phys. Rev. B **81**, 224503 (2010).

[31] P. Vilmercati, A. Fedorov, I. Vobornik, U. Manju, G. Panaccione, A. Goldoni, A. S. Sefat, M. A. McGuire, B. C. Sales, R. Jin *et al.*, Phys. Rev. B **79**, 220503 (2009).

[32] J. S. Kim, G. N. Tam, and G. R. Stewart, Phys. Rev. B **91**, 144512 (2015).

[33] L. Harnagea, S. Singh, G. Friemel, N. Leps, D. Bombor, M. Abdel-Hafiez, A. U. B. Wolter, C. Hess, R. Klingeler, G. Behr *et al.*, Phys. Rev. B **83**, 094523 (2011).

[34] R. Hu, S. L. Bud'ko, W. E. Straszheim, and P. C. Canfield, Phys. Rev. B **83**, 094520 (2011).

[35] J.-Q. Yan, A. Kreyssig, S. Nandi, N. Ni, S. L. Bud'ko, A. Kracher, R. J. McQueeney, R. W. McCallum, T. A. Lograsso, A. I. Goldman, and P. C. Canfield, Phys. Rev. B **78**, 024516 (2008).

[36] J. S. Kim, S. Khim, H. J. Kim, M. J. Eom, J. M. Law, R. K. Kremer, J. H. Shim, and K. H. Kim, Phys. Rev. B **82**, 024510 (2010).

[37] A. Thaler, H. Hodovanets, M. S. Torikachvili, S. Ran, A. Kracher, W. Straszheim, J. Q. Yan, E. Mun, and P. C. Canfield, Phys. Rev. B **84**, 144528 (2011).

[38] G. F. Chen, Z. Li, J. Dong, G. Li, W. Z. Hu, X. D. Zhang, X. H. Song, P. Zheng, N. L. Wang, and J. L. Luo, Phys. Rev. B **78**, 224512 (2008).

[39] K. Sasmal, B. Lv, B. Lorenz, A. M. Guloy, F. Chen, Y.-Y. Xue, and C.-W. Chu, Phys. Rev. Lett. **101**, 107007 (2008).

[40] N. P. Butch, S. R. Saha, X. H. Zhang, K. Kirshenbaum, R. L. Greene, and J. Paglione, Phys. Rev. B **81**, 024518 (2010).

[41] I. Pallecchi, F. Caglieris, and M. Putti, Supercond. Sci. Technol. **29**, 073002 (2016).

[42] E. D. Mun, S. L. Bud'ko, N. Ni, A. N. Thaler, and P. C. Canfield, Phys. Rev. B **80**, 054517 (2009).

[43] Y. J. Yan, X. F. Wang, R. H. Liu, H. Chen, Y. L. Xie, J. J. Ying, and X. H. Chen, Phys. Rev. B **81**, 235107 (2010).

[44] See Supplemental Material at http://link.aps.org/supplemental/10.1103/PhysRevB.97.054514 for Hall effect, Curie-Weiss analysis of susceptibility, and effect of annealing on T_c in the volume susceptibility.

[45] Y. Texier, Y. Laplace, P. Mendels, J. T. Park, G. Friemel, D. L. Sun, D. S. Inosov, C. T. Lin, and J. Bobroff, Europhys. Lett. **99**, 17002 (2012).

[46] P. F. S. Rosa, T. M. Garitezi, C. Adriano, T. Grant, Z. Fisk, R. R. Urbano, R. M. Fernandes, and P. G. Pagliuso, J. Appl. Phys. **115**, 17 (2014).

[47] G. S. Tucker, D. K. Pratt, M. G. Kim, S. Ran, A. Thaler, G. E. Granroth, K. Marty, W. Tian, J. L. Zarestky, M. D. Lumsden *et al.*, Phys. Rev. B **86**, 020503 (2012).

[48] E. D. L. Rienks, T. Wolf, K. Koepernik, I. Avigo, P. Hlawenka, C. Lupulescu, T. Arion, F. Roth, W. Eberhardt, U. Bovensiepen, and J. Fink, Europhys. Lett. **103**, 47004 (2013).

[49] J. A. Osborn, Phys. Rev. **67**, 351 (1945).

[50] B. Saparov and A. S. Sefat, Dalton Trans. **43**, 14971 (2014).

[51] S. R. Saha, N. P. Butch, K. Kirshenbaum, and J. Paglione, Phys. Rev. B **79**, 224519 (2009).

[52] J. Li, Y. F. Guo, S. B. Zhang, J. Yuan, Y. Tsujimoto, X. Wang, C. I. Sathish, Y. Sun, S. Yu, W. Yi *et al.*, Phys. Rev. B **85**, 214509 (2012).

[53] D. LeBoeuf, Y. Texier, M. Boselli, A. Forget, D. Colson, and J. Bobroff, Phys. Rev. B **89**, 035114 (2014).

[54] M. N. Gastiasoro and B. M. Andersen, Phys. Rev. Lett. **113**, 067002 (2014).

[55] K. Rogacki, B. Batlogg, J. Karpinski, N. D. Zhigadlo, G. Schuck, S. M. Kazakov, P. Wägli, R. Puźniak, A. Wiśniewski, F. Carbone *et al.*, Phys. Rev. B **73**, 174520 (2006).

[56] F. Hammerath, P. Bonfà, S. Sanna, G. Prando, R. De Renzi, Y. Kobayashi, M. Sato, and P. Carretta, Phys. Rev. B **89**, 134503 (2014).

[57] M. Sato, Y. Kobayashi, S. Lee, H. Takahashi, E. Satomi, and Y. Miura, J. Phys. Soc. Jpn. **79**, 014710 (2010).

[58] M. N. Gastiasoro, F. Bernardini, and B. M. Andersen, Phys. Rev. Lett. **117**, 257002 (2016).

[59] P. Cheng, B. Shen, J. Hu, and H.-H. Wen, Phys. Rev. B **81**, 174529 (2010).